Applied Catalysis B: Environmental 320 (2023) 121915

Contents lists available at ScienceDirect

Applied Catalysis B: Environmental

journal homepage: www.elsevier.com/locate/apcatb

Phase-separated CuAg alloy interfacial stress induced Cu defects for efficient N_2 activation and electrocatalytic reduction

Zengxi Wei [a,1], Zhengxiang Gu [b,1], Yechuan Zhang [c], Kui Luo [b,*], Shuangliang Zhao [a,*]

[a] Guangxi Key Laboratory of Petrochemical Resource Processing and Process Intensification Technology and School of Chemistry and Chemical Engineering, Guangxi University, Nanning 530004, China

[b] Huaxi MR Research Center (HMRRC), Department of Radiology, State Key Laboratory of Biotherapy, West China Hospital, Sichuan University, Chengdu 610041, China

[c] School of Chemical Engineering and Advanced Materials, University of Adelaide, SA 5005, Australia

A R T I C L E I N F O

Keywords:
Electrocatalyst
Nitrogen reduction reaction
Phase-separated CuAg alloy
Interfacial stress
Defects

A B S T R A C T

The electrochemical nitrogen reduction reaction (eN_2RR) to produce ammonia represents a promising approach to substitute the traditional Haber-Bosch process. However, it remains challenging due to the low ammonia yield caused by low Faradic Efficiency over the target intermediates. Herein, the adjacent Cu defect formed at the interface of phase-separated CuAg alloy was successfully prepared by using the cation-exchange method and identified as the most active electrocatalytic center for efficient N_2 reduction. The phase-separated CuAg alloy with rich interfacial Cu defective sites exhibited excellent eN_2RR performance with an ammonia production rate (38.35 μg h^{-1} cm^{-2}) and a Faradaic efficiency of 12.72 % at − 0.60 V versus reversible hydrogen electrode. Our work unravels fundamental principles for the rational design of electrocatalysts, and provides a strategy for fabricating the CuAg-PS alloy with rich interfacial Cu defective sites for eN_2RR.

1. Introduction

Nitrogen (N) is one of the most important elements for all living creatures since it provides proteins that are the building blocks of life. Nitrogen chemistry plays an indispensable role in sustaining life and various industrial processes [1–4]. The artificial reduction of abundant atmospheric nitrogen for its further transformation into ammonia (NH_3), nitric acid (HNO_3), and other valuable chemicals remains a key challenge of nitrogen chemistry [5,6]. The electrochemical N_2 reduction reaction (eN_2RR) can be processed under ambient condition and use inexpensive aqueous electrolytes as the proton source, and thus it is regarded as a promising alternative approach [7]. The direct electron transfer from electrode surface to N≡N requires overcoming substantially high energy barriers [8], and thus the key to achieve efficient N_2 reduction is to develop electrocatalysts with active catalytic centers that can efficiently reduce the large activation barrier of N≡N and promote its dissociation [9–11]. As an overwhelming level of water molecules exists than solvated N_2, the other key to achieve this goal is to enrich the electrocatalytic centers with defect sites that have significant higher selectivity for the N_2RR than the hydrogen evolution reaction (HER) [12].

For the six-electron process of electrochemical NH_3 synthesis, efficient catalyst with high Faradaic efficiency for nitrogen reduction reaction is a prerequisite [13,14]. Both theoretical and experimental studies have demonstrated the electrochemical synthesis of NH_3 using noble metallic catalysts (e.g., Ru, Rh, Au, and Pd) [15–18]. However, the high cost and natural scarcity of noble metals severely restrict their practical applications. Meanwhile, there is still tremendous room to further improve their performance to realize NH_3 production on an industrial scale [19–21]. To this end, one promising strategy is to alloy two metals to form bimetallic structure, which can modify the electronic structure of metals and thus change the adsorption energy of reactant species on the metals [22–24]. For instance, amorphous PdCu nanoclusters anchored on graphene have been developed for electrocatalytic nitrogen reduction to obtain ammonia [25], which displayed better performance than that of monometallic counterparts. Notably, theoretical investigations have demonstrated that Cu acts as one of the most active sites for electrochemical ammonia production [26–28], and it is thus expected that the Cu-based bimetallic structure is a promising candidate for electrocatalytic nitrogen reduction. Another typical

* Corresponding authors.
E-mail addresses: luokui@scu.edu.cn (K. Luo), szhao@gxu.edu.cn (S. Zhao).

[1] These two authors contributed equally to this work.

https://doi.org/10.1016/j.apcatb.2022.121915
Received 10 July 2022; Received in revised form 20 August 2022; Accepted 25 August 2022
Available online 31 August 2022

strategy for promoting the eN_2RR performance is to tailor the phase-separated atomic sites of electrocatalysts [29]. Phase-separated metallic materials with interconnected atomic nanoscale dislocation have great potential applications and facilitate transfer channels for adsorption/reaction of target species, thereby promoting the catalytic performance [30–33]. However, till date, the lack of bimetallic catalysts with phase-separated arrangement of respective metal atoms has prevented the study of structure effect (different mixing patterns of two elements) on productive rate. In addition, the study of phase-separated CuAg alloy with interface for the application of eN_2RR is limited. The interface energy is found to be vital in forming the nucleation barrier and preferential orientation of interfacial atoms [34]. It is acknowledged that the interface intends to form along the crystal face with lowest energy based on previous theoretical calculations [35]. Surface effect of small nanoparticles on determining the main energetic landscape should be illustrated based on the study of surface energy [36]. In fact, it is more likely to produce abundant defect sites at the alloy interface structure with high surface energy, which is conducive to the electrochemical reactions [37–39]. However, the alloy interface with high surface energy is rarely reported. The synergistic effects of interface energies and surface energies of different crystalline planes on forming the nanostructure of CuAg alloy and its corresponding function of catalyzing eN_2RR have not been well demonstrated.

Herein, by means of density function theory (DFT) calculations, we first identified that the phase-separated CuAg alloy electrocatalyst can chemically adsorb and then activate N_2 molecules in a lying-down manner, especially for the specific adsorption of N_2H^* intermediates at the interface of the phase-separated CuAg alloy (Fig. 1). The theoretical calculation also indicated the relationship between the surface energy of crystalline planes and the formation of interface in CuAg-PS. Benefited from the phase-separated property and bimetallic composition, the as-prepared CuAg alloy can be directly utilized as an eN_2RR catalyst, which exhibits enhanced performance toward ammonia production, compared with monometallic Cu and Ag catalysts under ambient condition. Electrochemical measurements demonstrated that the phase-separated CuAg alloy exhibited significant enhanced eN_2RR performances, including an ammonia formation rate of 38.35 μg h^{-1} cm^{-2} and a corresponding Faradaic Efficiency (FE_{NH_3}) of 12.72%, significantly surpassing those of undoped Cu nanowires or commercial Cu and Ag powder, whose efficiencies were limited by their lower N_2H^* adsorptive capability.

2. Experimental section

2.1. Materials

Pure copper film (Cu, 99.5 %, Sinopharm Chemical Reagent Co.), $AgNO_3$ ($AgNO_3$, 99 %, Sinopharm Chemical Reagent Co.), pure silver (Ag, 99.5 %, Sinopharm Chemical Reagent Co.), hydrochloric acid (HCl, 35.0~38.0 %, Beijing Chemical Works), absolute ethyl alcohol (C_2H_5OH, Beijing Chemical Works), sodium sulfate (Na_2SO_4, 99%, Sinopharm Chemical Reagent Co.), sodium hydroxide (NaOH, 96.0 %, Sinopharm Chemical Reagent Co.), salicylic acid ($C_7H_6O_3$, 99.5%, Sinopharm Chemical Reagent Co.), sodium hypochlorite solution (NaClO, available Cl 4.0 %, Shanghai Macklin Chemical Works), copper sulfate ($CuSO_4$, 99 %, Sinopharm Chemical Reagent Co.), sodium nitroferricyanide dehydrate ($C_5FeN_6Na_2O{\bullet}2\,H_2O$, 99.0 %, Sigma-Aldrich), ammonium chloride (NH_4Cl, 99.5 %, Sinopharm Chemical Reagent Co.; $^{15}NH_4Cl$, 99 atom %, Sigma-Aldrich), hydrazine monohydrate ($N_2H_4{\bullet}H_2O$, 99.0 %, Alfa Aesar), P-dimethylaminobenzaldehyde (PDAB, $C_9H_{11}NO$, 99 %, Adamas-beta Chemical Co.), dimethyl sulfoxide-d6 (DMSO-d6, deuterium for 99.9 %, Alfa Aesar), deuteroxide (D_2O,99.9 %, Sigma-Aldrich), dimethyl sulfoxide-d6 (DMSO-d6, deuterium for 99.9%, Alfa Aesar), nitrogen (N_2, high purity 99.999%, Ju' yang gas Co.), argon (Ar, high purity 99.999%, Ju' yang gas Co.), $^{15}N_2$ (enrichment of > 99 % atom ^{15}N, Shanghai Research Institute of Chemical Industry Co.), hydrogen peroxide (H_2O_2, 30 %, Beijing Chemical Works), fulfuric acid (H_2SO_4, 99 %, Beijing Chemical Works), deionized (DI) water with the specific resistance of 18.2 MΩ·m was obtained by reversed osmosis followed by ion-exchange and filtration. All chemical reagents were used as purchased without further purification.

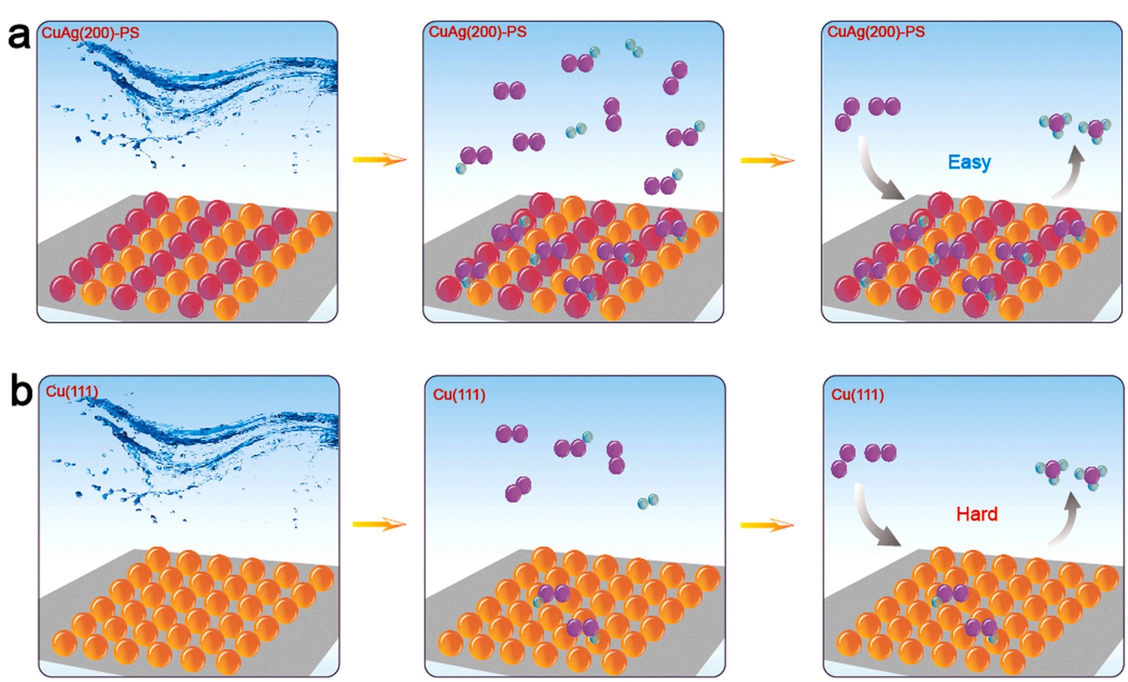

Fig. 1. Schematic of the as-synthesized Cu and CuAg(200)-PS alloy electrocatalysts and the subsequent eN_2RR process. (a) The phase-separated CuAg (CuAg(200)-PS) alloy electrocatalyst with plentiful favors to adsorb N_2H^* to promote ammonia production. (b) The electrochemical N_2 process of Cu catalyst with the low adsorption density of N_2H^* difficult to promote ammonia production.

2.2. Synthesis of Cu NWs

$Cu(OH)_2$ NWs were first synthesized on Cu foils by immersing Cu foils into a solution mixture containing 0.133 M $(NH_3)_2S_2O_8$ and 2.667 M NaOH. Cu NWs were then fabricated by annealing the $Cu(OH)_2$ NWs at 150 °C for 2 h in 5 %H_2/Ar.

2.3. Synthesis of CuAg alloy

0.3 g of polyvinylpyrrolidone (PVP) was added to 15 mL of glycol under magnetic stirring for 30 min. Afterwards, 5 mL glycol solution containing 0.11 g $AgNO_3$ were added to the previous solution dropwise under magnetic stirring for 2 h. Next, Cu nanowires grown on Cu foils were together added to the mixed solution, followed by the addition of 100 μL AgCl with continuous heating at 170 °C for 30 min. After washed with ethanol and DI water for 3 times, respectively, the obtained product was annealed with 5% H_2/Ar gas mixture at 300 °C for 2 h. The final product of CuAg alloy was obtained after it was cooled to room temperature.

2.4. Electrochemical measurements

The electrochemical tests were conducted in 0.05 M H_2SO_4 solution using an autolab electrochemical workstation (CH Instruments Inc., USA) with a three-electrode setup. A platinum foil and a saturated calomel electrode (SCE) were used as counter and reference electrodes, respectively. All potentials were referred to the RHE by adding a value of (0.2046 + 0.05917 × pH) V. For the working electrode, 2 mg of the sample was dispersed in 1 mL of ethanol and 0.12 mL of 5 wt% Nafion aqueous solution. The mixed solution was sonicated for 30 min to form a homogeneous ink. 120 μL of the ink was drop-casted onto carbon paper with an area of 0.5 cm^2, followed by drying under room temperature. Before electrolysis, the electrolyte was bubbled with high-purity N_2 gas (99.99 %) for 30 min to saturate in the solution. Linear sweep voltammetry (LSV) and cyclic voltammetry (CV) were carried out in a voltage window from –1.0–0 V vs. RHE at the scan rate of 1 and 120 mV s^{-1}, respectively. All the polarization curves were the steady-state ones after several CV cycles. The current density was normalized to the geometrical area.

2.5. Quantification of ammonia

The indophenol blue method was used to accurately measure the concentration of ammonia. 1.474 g of sodium hydroxide (NaOH) solid was dissolved in 100 mL of DI water, followed by adding 5 g of salicylic acid and 5 g of sodium potassium tartrate. The prepared solution was a color reagent. 0.1 g of sodium nitroprusside was dissolved in 10 mL of DI water to form a sodium nitroprusside solution. 1.5 g of sodium hydroxide was added into 50 mL of sodium hypochlorite solution. In the color test, 8 mL of the electrolyte (after the N_2RR test) was added into a 10-mL colorimetric tube, with the following solutions: including 1 mL of color reagent, 500 μL of NaOH solution (4 M), 100 μL of sodium nitroprusside solution, and 100 μL of sodium hypochlorite solution, and 300 μL of DI water. The mixed solution was set aside for 1 h, before the UV-Vis measurements performed at 660 nm.

The quantity of NH_3 formation was determined via a colorimetric method using Nessler's reagent. First, preparing a series of reference solutions, by pipetting suitable volumes of the ammonia-nitrogen working 0.1 M KOH solution in colorimetric tubes; Second, making up to the mark (10 mL) with 0.1 M KOH solution; Third, adding 1 mL of 0.2 M potassium sodium tartrate ($KNaC_4H_4O_6$, chelating soluble metal ion) ultrapure water solution to each of the tubes and mix thoroughly; Fourth, adding 1 mL of Nessler's reagent to each of the tubes and mix thoroughly; Fifth, allowing the solutions to sit for 20 min for color development; Sixth, performing background correction with a blank solution and measuring the absorbance of the solutions at 425 nm using a 10 mm glass cuvette.

2.6. Quantification of hydrazine

The amount of hydrazine was measured based on the condensation of hydrazine with 4-(dimethylamino) benzaldehyde. 5.99 g of p-dimethylbenzaldehyde was dissolved in 30 mL of hydrochloric acid(36.0 ~ 38.0 %) and 300 mL of ethanol, as a colour reagent. For the colour test, 5 mL of the test solution and 5 mL of the colour reagent were added into a 10-mL colorimetric tube, and set aside for 20 min. Then, the UV-Vis measurements were performed at 458 nm.

2.7. Faradaic efficiency

Faradaic efficiency of the ammonia production was calculated using the following equation: $FE_{NH3} = 3\ F \times m_{NH3} / (17 \times Q)$, where F is the Faraday constant, m_{NH3} is the measured NH_3 mass, and Q is the quantity of applied electricity.

2.8. Computational details

In this work, density functional theory calculations were performed by using the Vienna *Ab Initio* Simulation Package (VASP) [40–42]. To obtain the optimized structures, we set an energy cutoff, electron convergence energy and ionic relaxation to be 400 eV, 10^{-5} eV and 0.02 eV/Å, respectively. Bulk Ag was optimized using (6 ×6 ×6) k-points mesh, and bulk Cu was optimized using (7 ×7 ×7) k-points mesh. For the interfacial optimize, (3 ×3 ×1) and (2 ×2 ×1) k-points mesh are set for Ag(111), Ag(200), Cu(111), Cu(200) and CuAg(200)-PS alloy, respectively. A vacuum of at least 15 Å is used in these surface structures to avoid the interactions between its periodic images. The DFT-D3 scheme is adopted to correct the van der Waals interaction [43].

To reveal the Gibbs free energy for each reaction step, the computational hydrogen electrode (CHE) method was employed. Under standard conditions (298.15 K, 1 atm, pH=0), the free energy of H^+/e^- pair ($G(H^+ + e^-)$) is equivalent to that of a half of hydrogen ($1/2\ G(H_2)$) without applied bias (U). The reaction free energy is defined as:[20].

$$\Delta G = \Delta E + \Delta ZPE - T\Delta S$$

where ΔE, ΔZPE and ΔS stand for the reaction energy, differences in zero point energy and entropy, respectively. With an applied bias (U), the reaction free energy can be described as:

$$\Delta G = \Delta E + \Delta ZPE - T\Delta S - neU$$

where n is the number of electrons involved in the reaction.

3. Results and discussion

3.1. Preparation and characterization of catalysts

The as-synthesized Cu_2O nanowires are uniformly grown with an average diameter of 100–200 nm and a length of 20–50 μm (Fig. S1). Cu nanowire exhibited a nanowire structure with a smooth surface and a layer of thin film (Fig. 2a). The atomic structures were characterized by high resolution transmission electron microscopy (HRTEM, Fig. 2b). Ordered Cu lattice (111 plane) was observed in Cu nanowires with the lattice spacing of 0.207 nm (Fig. 2c). For the CuAg-PS alloy, it exhibited tubular structures with a rough surface and attached flakes, revealed by the contrast of dark and light areas (Fig. 2d, e). According to HRTEM measurements (Fig. 2f), the CuAg-PS alloy showed a high crystallinity with the lattice spacing of 0.211, 0.181, 0.233, and 0.208 nm, corresponding with Cu(111, 200), Ag(111), and Ag(200) planes, respectively. Geometric phase analysis was adopted to analyze the presence of lattice strain, which is reflected by the variation of lattice plane, thus leading to the occurrence of interfacial stress [44]. Both horizontal strain (E_{xx}) and

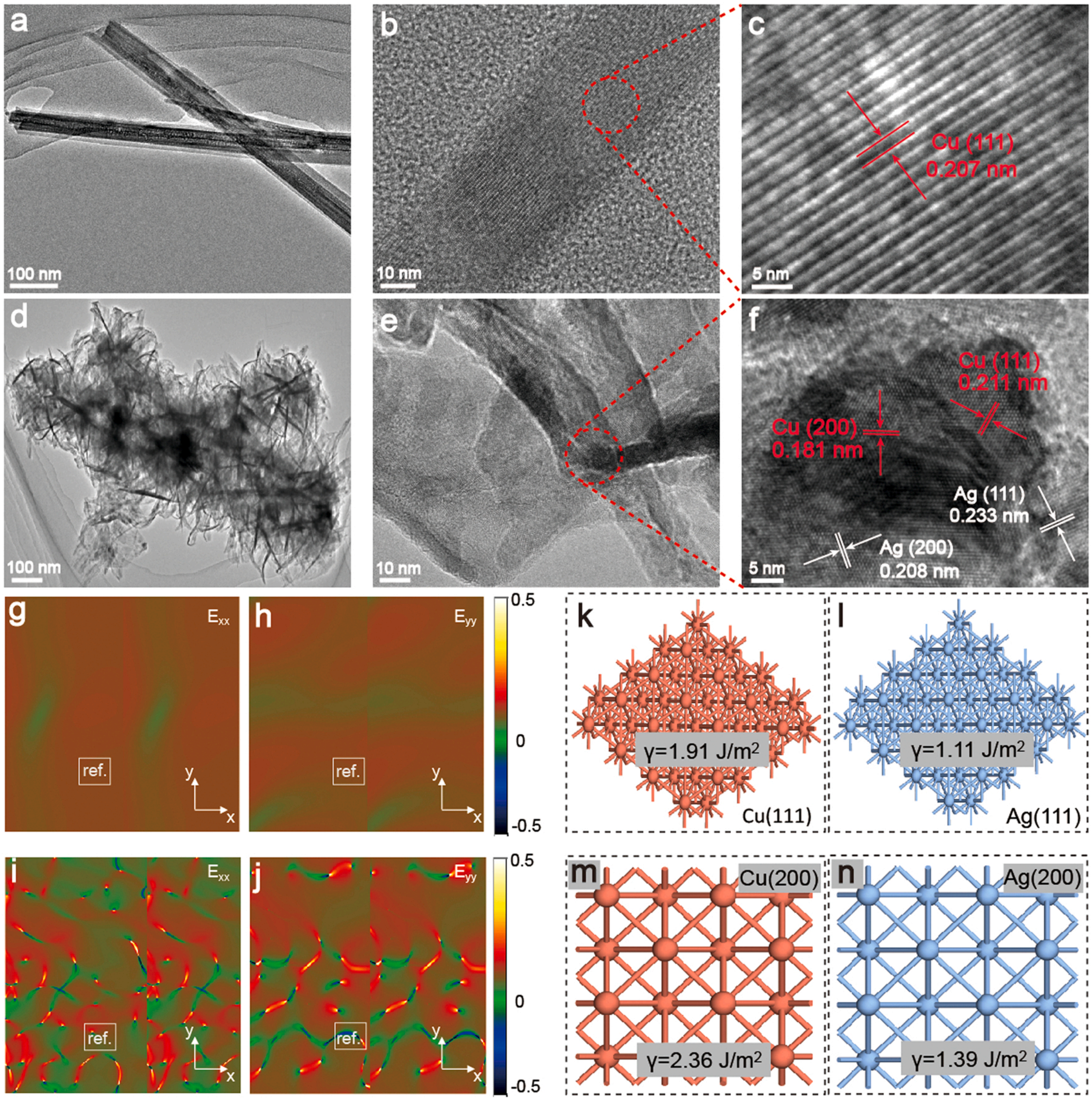

Fig. 2. Structure characterizations of Cu and CuAg-PS alloy. (a) Low resolution TEM image of Cu nanowire. (b, c) High resolution TEM image of Cu nanowire. (d) Low resolution TEM image of CuAg-PS alloy. (e, f) High resolution TEM image of CuAg-PS alloy. (g, h) GPA analysis in c of horizontal normal strain (E_{xx}) and vertical normal strain (E_{yy}). (i, j) GPA analysis in f of horizontal normal strain (E_{xx}) and vertical normal strain (E_{yy}). Surface energies of (k) Cu(111), (l) Ag(111), (m) Cu(200) and (n) Ag(200), respectively.

vertical strain (E_{yy}) emerged along the Cu nanowire and CuAg-PS alloy. As shown in Fig. 2g-h, the clear and sole (111) lattice plane on Cu nanowire, suggested the weak elastic strain is pervasive on its surface, which is ascribed to the known surface tension. Thus, both the horizontal strain (Fig. 2g) and vertical strain (Fig. 2h) exhibited inconspicuous strain on the Cu(111) surface. However, this calm state was disturbed by the introduction of Ag. Experimental results demonstrated that the alloying processes of Cu and Ag facilitated the formation of the special alloy interface between Cu(200) and Ag(200) (Fig. 2i-j). Geometric phase analysis proved that both horizontal strain (Fig. 2i) and vertical strain (Fig. 2j) occurs at the CuAg(200)-PS alloy interface with a maximum value of ~0.2%. In fact, the remarkable interfacial stress of CuAg(200)-PS alloy plays a key role in regulating the interfacial structure (i.e., metal defects) and electrocatalytic activity. Moreover, it is also noteworthy that the formation of the identified CuAg(200)-PS alloy interface could be ascribed to the higher surface energies of Cu(200) and Ag(200) lattice plane than that of Cu(111) and Ag(111), respectively, as illustrated in Fig. 2k-n. More details are discussed in the DFT calculation section.

The X-ray diffraction (XRD) of CuAg-PS alloy and the Cu nanowire was conducted to investigate the structural changes caused by the introduction of Ag, in which both samples displayed high crystallinities (Fig. 3a). The intensity ratios of Cu(200) and Cu(111) peaks of CuAg-PS alloy was lower than that of Cu foil and Cu nanowire, indicating that Cu and Ag were (111)-oriented in CuAg-PS alloy sample [45]. To gain insight into the electronic structures, the X-ray photoelectron spectroscopy (XPS) was conducted to investigate the chemical states. The actual Cu/Ag ratio in the sample was readily tuned and determined by inductively coupled plasma mass spectrometry (ICP-MS) (Table S1 in the SI). The ratio of Cu/Ag at the surface was found to be similar to the bulk, confirming that Ag dopants were evenly distributed in the CuAg catalyst. The binding energy (B.E.) of Cu $2p_{3/2}$ shifted from 932.1 eV (in Cu nanowire) to 932.6 eV (CuAg-PS alloy, Fig. 3b). Identical trends were observed for Cu $2p_{1/2}$ peaks with a shift of binding energy from 951.1 eV (Cu nanowire) to 951.3 eV (CuAg-PS alloy, Fig. 3b). This binding energy shift of Cu was attributed to the interphase electron transfer from Cu to Ag atoms, resulting from the electron deficiency Cu atoms (i.e., electron donor) [46]. Nevertheless, the binding energy of Ag presented a reverse

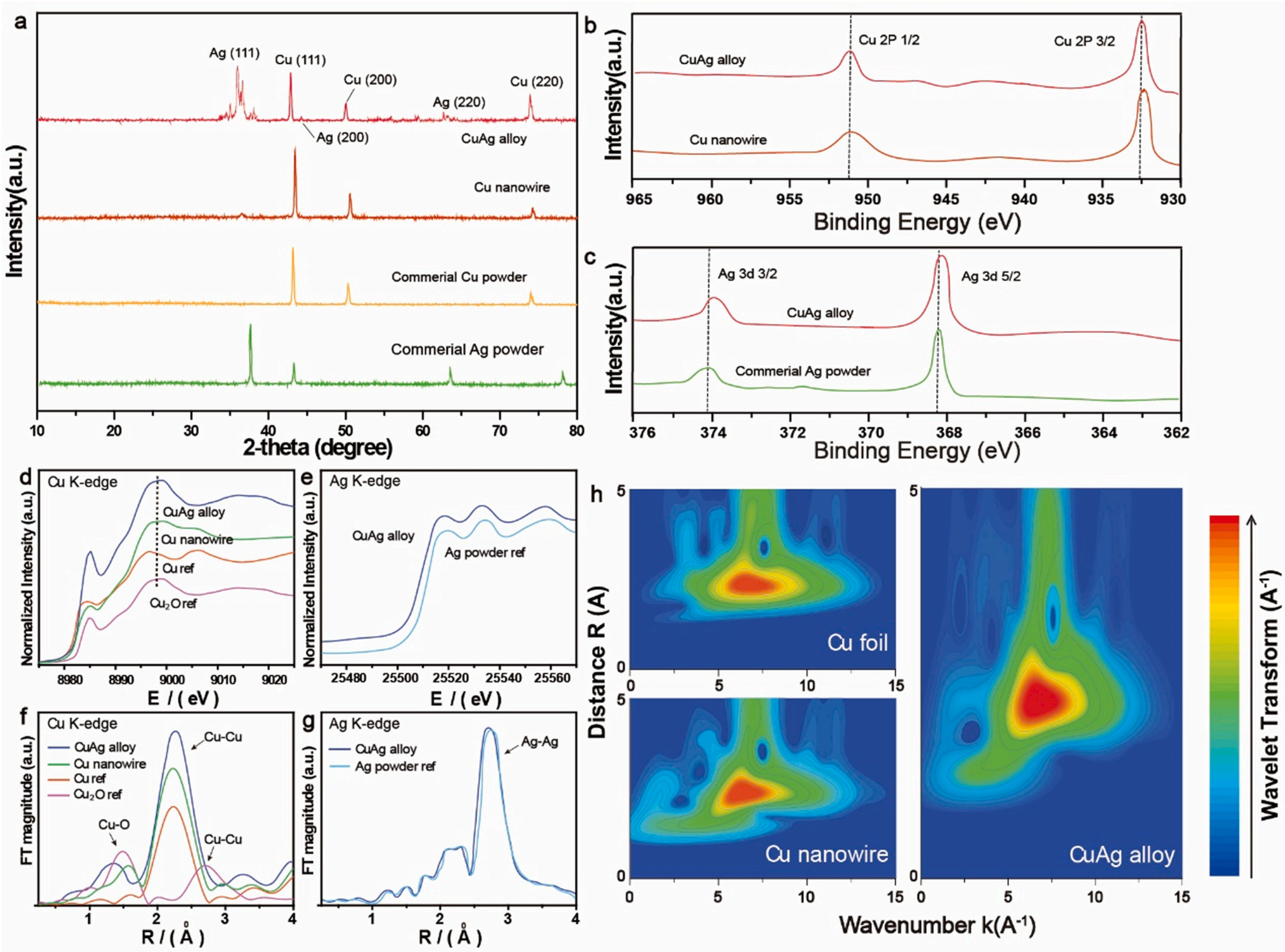

Fig. 3. (a) XRD patterns of the as-prepared samples. XPS spectra of (b) Cu 2p and (c) Ag 3d for Cu nanowire, commercial Ag powder, and CuAg alloy samples. (d) Cu K-edge XANES spectra of CuAg-PS alloy, Cu nanowire and reference samples (Cu and Cu_2O) (e) Ag K-edge XANES spectra of CuAg-PS alloy and reference samples of Ag powder. (f) FT magnitudes of Cu K-edge EXAFS for CuAg-PS alloy, Cu rod, and the reference samples. (g) FT magnitudes of Ag K-edge EXAFS for CuAg-PS alloy and the reference samples. (h) WTs for CuAg-PS alloy, Cu foil and Cu nanowire.

shifting trend (Fig. 3c). Ag $3d_{3/2}$ and $3d_{5/2}$ peaks shifted from 373.9 and 368.1 eV (in CuAg-PS alloy) to 374.2 and 368.3 eV (in Cu nanowire), respectively. To better understand the interaction between Cu and Ag, the X-ray absorption near-edge structure (XANES) and extended X-ray absorption fine structure (EXAFS) were further conducted. The XANES spectra at Cu K-edge confirmed that the edge features of as-synthesized Cu nanowire and CuAg-PS alloy samples, which were identical to those of commercial Cu reference (dot lines in Fig. 3d), indicating the existence of major copper phase. A similar phenomenon was observed for silver (Fig. 3e). The corresponding Fourier transform curves for the first coordination shell illustrated that the Cu-Cu coordination located at ≈ 2.3 Å was the dominant structure of each sample (Fig. 3f). In terms of Ag (Fig. 3g), the Ag-Ag distance in the first shell is 2.74 Å, shorter than that of 2.75 Å in Ag powder reference, which indicated the existence of lattice distortion and coordination deficiency in the CuAg-PS alloy sample, further verifying the change of electronic structure in the format of bonding (Fig. 3h), which resulted from the phase-separated nature of CuAg alloy catalyst [47].

3.2. Theoretical investigation

In order to illustrate the outstanding performance of CuAg-PS alloy for the eN_2RR, DFT calculations combining with experimental results were analyzed to explore the mechanism related to its structure from the atomic perspective. The experimental results identified the growing preferential of (111) and (200) lattice plane in Cu and Ag. The HRTEM suggested that CuAg(200)-PS is the leading part of the CuAg alloy. We first discussed the eN_2RR activity on the surface of Cu and Ag, respectively. The calculation results suggested that the first hydrogenation step from adsorbed N_2 to form $*N_2H$ is the rate-determining step (RDS) during the eN_2RR processes on the CuAg(200)-PS alloy interface. For the (111) lattice plane, the Cu(111) surface needs to overcome the free energy barrier of 1.78 eV to release ammonia one by one (Fig. 4c and Fig. S2). The ammonia production on the Ag(111) surface is endothermic, requiring 2.02 eV for the eN_2RR processes (Fig. 4c and Fig. S3). When the N_2 is activated and reduced on the high index lattice plane of (200), the reaction free energies were decreased obviously. For the Cu (200) surface, the first hydrogenation process has an uphill energy of 1.19 eV, which is decreased by 0.6 eV than that on the Cu(111) surface (Fig. 4c and Fig. S4). Similarly, compared with the Ag(111) surface, the Ag(200) surface has to overcome a lower free energy of 1.59 eV for production of ammonia (Fig. 4c and Fig. S5). It is clear that the eN_2RR activity on Cu and/or Ag catalyst follows the trend Cu(200) > Ag(200) > Cu(111) > Ag(111). The structure-activity relationship of Cu or Ag catalyst can be ascribed to the high index crystal face with higher surface energy and higher activity, as displayed in Fig. 2k-n [48]. For example, the Cu(200) surface has the higher surface energy (2.36 J/m^2) than that on the Cu(111) surface (1.91 J/m^2), whereas the surface energy of Ag

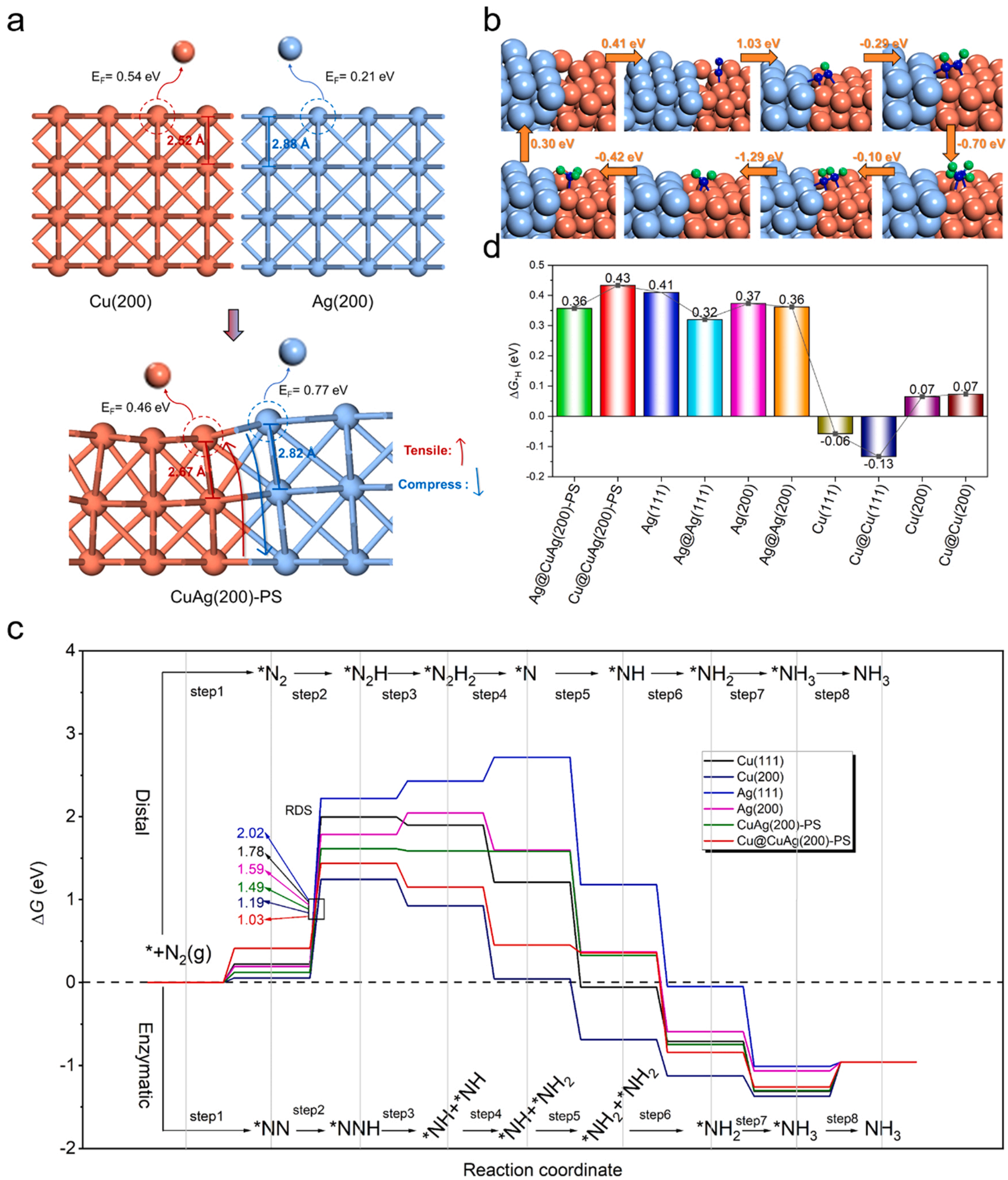

Fig. 4. Electrochemical nitrogen reduction reaction mechanism. (a) Tensile and compress strain at CuAg-PS alloy interface. And the formation mechanism of Cu defect at CuAg-PS alloy interface. (b) Optimized geometries of eN_2RR processes on CuAg(200)-PS alloy catalyst. And the Gibbs free energies are given for each step. (c) Free energy diagrams of eN_2RR on Cu(111), Cu(200), Ag(111), Ag(200), CuAg(200)-PS, and Cu@CuAg(200)-PS, respectively. (d) Adsorption free energies of hydrogen on Cu(111), Cu@Cu(111), Cu(200), Cu@Cu(200), Ag(111), Ag@Ag(111), Ag(200), Ag@Ag(200), Cu@CuAg(200)-PS and Ag@CuAg(200)-PS, respectively.

(200) (0.28 J/m^2) is lower than that of Ag (111) (1.11 J/m^2).

To better address the function and the corresponding mechanism of the CuAg(200)-PS alloy interface, the structure-activity relationship was illustrated based on the computational and experimental results. According to the above discussion, the CuAg(200)-PS alloy heterogeneous structure with interfaces is dominant in the catalytic process of eN_2RR. We first construct an optimized CuAg(200)-PS alloy interface by using DFT calculations. According to calculation results, the interfacial lattice between Cu(200) and Ag(200) causes a nonnegligible stress (Fig. 4a). The interfacial Cu-Cu bond is stretched from the initial 2.52–2.67 Å, and the Ag-Ag bond is distorted by 0.06 Å, which is in good agreement with the experimental results in Fig. 3. The stretching stress suggested that the interfacial Cu atoms are more vibrant than Cu atoms not at the interface. The formation energy of Cu defect at the interface is 0.46 eV, which is smaller than that on Cu(200) surface (0.54 eV). On the contrary, the Ag defect formation energy at the interface is 0.56 eV, larger than that on the Ag(200) surface (0.21 eV). Thus, the Cu defect is inclined to form at the CuAg(200)-PS interface, denoted as Cu@CuAg (200)-PS. Without interfacial defects, the reaction free energy of eN_2RR were first calculated. As can be seen in Fig. S6, the N_2 adsorption on CuAg(200)-PS alloy interface is distal configuration, which is the same as that on pristine Cu or Ag surface (i.e., Cu(200), Cu(111), Ag (200), Ag(111)). The first hydrogenation process requires an uphill energy barrier of 1.49 eV to form $*N_2H$, which is the RDS for the production of ammonia. It is worth noting that the reaction energy barrier of eN_2RR on CuAg(200)-PS alloy interface is 0.3 eV larger than that on

Cu(200) surface. This may result from the tensile stress of Cu atoms at the interface, leading to the weak adsorption of the intermediate of $*N_2H$. The calculation results demonstrated that the adsorption free energy of $*N_2H$ on CuAg(200)-PS alloy interface is 0.35 eV larger than that on Cu(200) (1.24 eV). Consequently, the defect-free CuAg(200)-PS alloy interface is not beneficial for NH_3 production.

After introducing the Cu defect on the CuAg(200)-PS alloy interface, the reaction pathway of eN_2RR at the Cu@CuAg(200)-PS alloy interface obeys the enzymatic mechanism. As shown in Fig. 4b, the N_2 molecule was adsorbed on the Cu@CuAg(200)-PS alloy interface by a side-on configuration with the adsorption free energy of 0.41 eV. Subsequent hydrogenation process to form *NNH intermediate needs to overcome the reaction energy barrier of 1.03 eV, which is the RDS of eN_2RR processes (Fig. 4c). It found that the reaction free energy of eN_2RR on Cu@CuAg(200)-PS alloy interface is 0.46 eV, smaller than that on CuAg (200)-PS alloy interface, which can be attributed to stress-induced Cu defects. As a comparison, the reaction free energy of Ag defects at the CuAg(200)-PS alloy interface is investigated. The calculation results exhibited that the reaction free energy of the eN_2RR at Ag@CuAg(200)-PS alloy interface is ~1.0 eV (Fig. S7). Although the Ag@CuAg(200)-PS alloy interface has a lower reaction energy than that at Cu@CuAg(200)-PS alloy interface, the entire reaction is limited by the higher Ag defect formation energy. In addition, after introducing Cu or Ag defect on the surface of Cu(200) or Ag(200), respectively, the eN_2RR on Cu@Cu(200) and Ag@Ag(200) were calculated and illustrated in the SI (Fig. S8 and Fig. S9). The free energy barrier of eN_2RR on Cu@Cu(200) is 0.03 higher than that on Cu (200), whereas the free energy barrier on Ag@Ag(200) surface is 0.06 smaller than that on Ag(200). As a result, the stress-induced defect at the CuAg(200)-PS alloy interface in the main factor of the highly efficient for ammonia production. Moreover, the

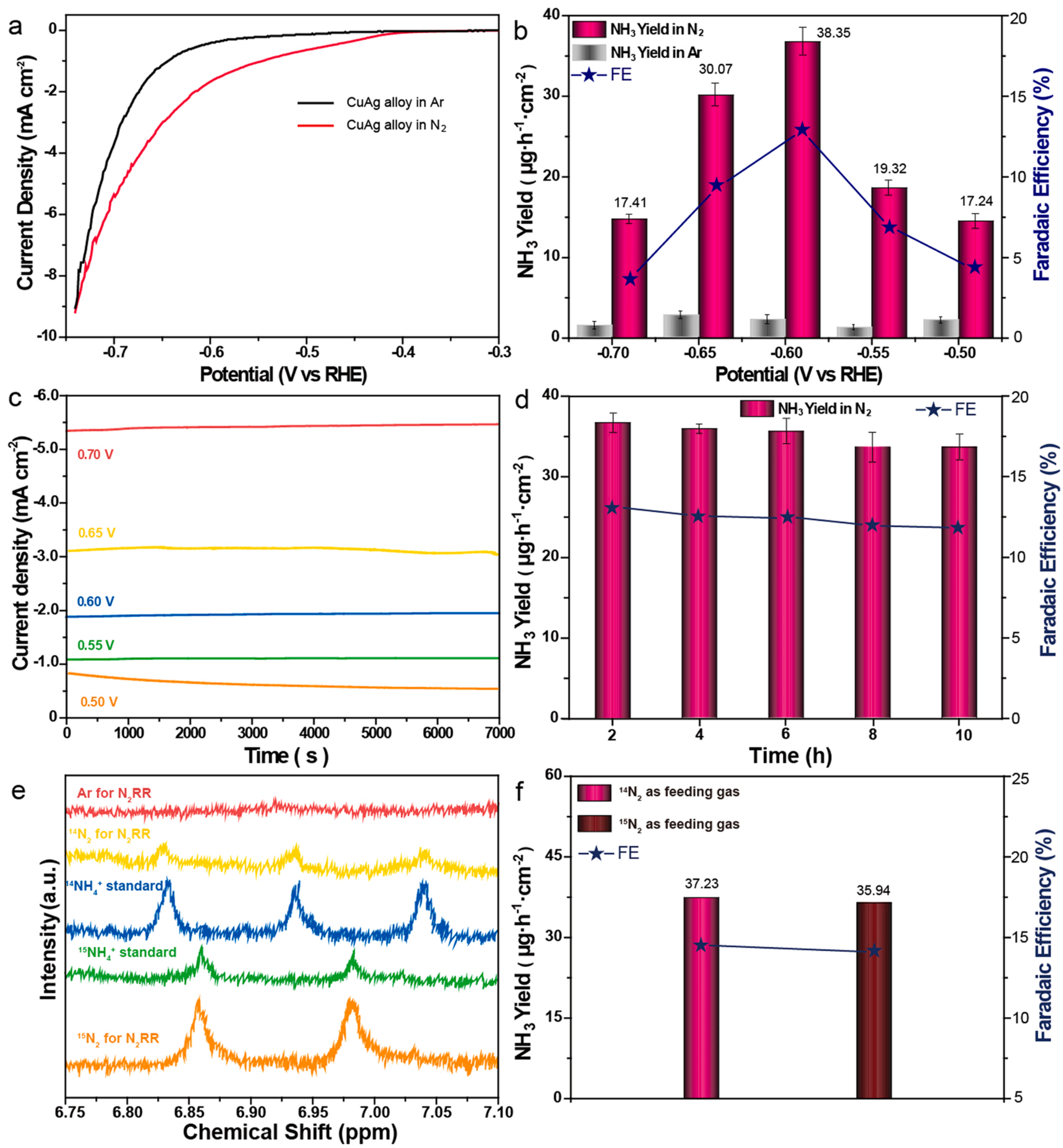

Fig. 5. eN_2RR performance of CuAg alloy catalyst. a) LSV curves of CuAg alloy in Ar- and N_2-saturated 0.1 M Na_2SO_4 (scan rate: 10 mV s^{-1}). (b) The NH_3 production rates (left y-axis) and FE_{NH_3} (right y-axis) of CuAg alloy under N_2 (red column) and Ar (gray column) atmosphere at various applied potentials between –0.5 and −0.7 V vs RHE. The error bars represent the average of three independent measurements. (c) Chronoamperometric curves of CuAg alloy at different applied potentials. (d) The eN_2RR stability test of CuAg alloy at – 0.60 V vs. RHE. (e) Isotopic labeling results from the eN_2RR at **− 0.60 V** versus RHE using Ar, $^{14}N_2$ or $^{15}N_2$ as the feeding gas and compared to the standard $^{14}NH_4^+$ and $^{15}NH_4^+$. (f) Comparison of the ammonia yield rate and NH_3 Faradaic efficiencies using different feeding gases for the eN_2RR at − 0.60 V vs. RHE.

competitive hydrogen evolution reaction (HER) is also analyzed. As shown in Fig. 4d, a weak hydrogen adsorption free energy at the Cu@CuAg(200)-PS alloy interface (~0.43 eV) suggested the production of NH_3 is predominant during the eN_2RR, rather than the unfriendly side reaction (HER). However, the strongest hydrogen adsorption free energy is on the surface of Cu@Cu(111) with a value of − 0.13 eV.

3.3. Electrochemical investigation

The electrochemical eN_2RR was then evaluated in the 0.05 M H_2SO_4 solution saturated with N_2 or Ar, using a standard three-electrode electrochemical setup (Experimental section). All the potentials below were converted and reported as values versus RHE. In order to minimize the experimental errors in quantifying ammonia yield rate and corresponding FE, the current density threshold was set as 0.1 mA cm^{-2} to indicate the onset of electrochemical reactions [45]. Fig. 5a showed the linear sweep voltammetry (LSV) curves of the CuAg-PS alloy in Ar-and N_2-saturated 0.1 M H_2SO_4 solutions, respectively. The linear sweep voltammetry (LSV) curve of the CuAg-PS alloy sample in the N_2-saturated electrolyte presented a higher (negative) current density than that in the Ar-saturated electrolyte, indicating that the current density was increased by the eN_2RR itself. In contrast, the LSV curves of the Cu nanowire sample showed minor difference regarding the current density using N_2 and Ar saturated electrolytes (Fig. S10). The product of the eN_2RR was determined by analyzing the composition of electrolyte after 2 h of the continuous electrolysis at different selected potentials. The amount of two N_2RR products, NH_3 and N_2H_4, were quantified by the sodium salicylate-sodium hypochlorite method and the 4-(dimethylamino) benzaldehyde spectrophotometric method, respectively [46]. The standard curves of ammonia and hydrazine are displayed in Fig. S11. To eliminate possible interferences on the product quantification, a series of control experiments were conducted as follows: (1) The working electrode with the CuAg-PS alloy catalyst was put in a N_2-saturated electrolyte, but with an open circuit for 2 h; (2) The working electrode with the CuAg-PS alloy catalyst was put in an Ar-saturated electrolyte with applied potentials for 2 h; (3) A carbon paper electrode was put in a N_2-saturated electrolyte with applied potentials for 2 h. In all these controls, the ammonia detected could not be differentiated with the background level (Table S2). Therefore, it is confirmed that the ammonia detected was produced by the electrochemical eN_2RR on the CuAg-PS alloy catalyst.

As observed in Fig. 5b, the CuAg-PS alloy catalyst tested under N_2 atmosphere showed both significant higher ammonia yield rates and corresponding FE_{NH_3} than those of tested under Ar atmosphere with various applied potentials between − 0.6 and − 0.8 V (Fig. 5b), revealing the NH_3 product are produced by the eN_2RR activity of the CuAg-PS alloy catalyst. At − 0.60 V, the CuAg-PS alloy catalyst exhibited a maximum ammonia production rate of 38.35 μg h^{-1} cm^{-2} with a maximum FE_{NH_3} value of 12.72% (Fig. 5b). The ammonia production was also quantified by the Nessler Reagent method (Fig. S12), showing a comparable result with the indophenol blue method. For N_2H_4, the CuAg-PS alloy catalyst presented a peak production rate of 2.8 μg h^{-1} cm^{-2} with a maximum $FE_{N_2H_4}$ value of 1.3 % (Fig. S13), exceeding those of the Cu nanowire. The eN_2RR performance of our CuAg-PS alloy sample was also compared with other metal catalysts reported in previous literature (Table S3). The CuAg-PS alloy catalyst in our work presented the top-level eN_2RR performance among various previously reported eN_2RR catalysts. Moreover, the chronoamperometric i-t curves of the CuAg-PS alloy were measured at different potentials between − 0.50 and − 0.70 V to verify its catalytic stability (Fig. 5c). The TEM images in (Fig. S14) clearly demonstrate the well-retained original morphology after the stability test indicated that CuAg-PS alloy possesses superior stability. The current densities were all maintained with good stability. The catalytic stability of the CuAg-PS alloy samples was further tested at − 0.60 V for 5 cycles (Fig. 5d). During the entire 10-h period, both the ammonia production rate and the corresponding FE_{NH_3} showed a decrease of less than 10 %, confirming the good stability of the CuAg-PS alloy catalyst. The eN_2RR tests of Cu rod exhibited a peak ammonia production rate of 13.63 μg h^{-1} cm^{-2} with a maximum FE_{NH_3} value of 5.26 % (Fig. S15), showing higher NH_3 yield rate and FE of bimetallic CuAg-PS than those of Cu nanowire, also suggesting that the synergistic effect of Cu and Ag plays an important role in improving the eN_2RR activity. To further verify the N source of the obtained NH_3, the isotopic labeling experiment using $^{14}N_2$ and $^{15}N_2$ as the feeding gas was performed [47]. As shown in Fig. 5e, only two peaks corresponding to $^{15}NH_4^+$ are observed when using $^{15}N_2$ as the feeding gas. In contrast, there are three peaks corresponding to $^{14}NH_4^+$ when using $^{14}N_2$ as the feeding gas. In addition, no signal of $^{15}NH_4^+$ or $^{14}NH_4^+$ can be detected when using Ar as the feeding gas. These results further confirm that the detected NH_3 is produced via an electrochemical eN_2RR. Moreover, the obtained ammonia production rate and the corresponding FE_{NH_3} of using $^{15}N_2$ as the feeding gas are comparable to those of using $^{14}N_2$ (Fig. 5f), confirming that the obtained ammonia is produced from the electroreduction of N_2.

4. Conclusion

In summary, we have presented a theory-guided design of CuAg-PS alloy for electrocatalytic N_2 reduction to NH_3. The theoretical calculation indicates that alloying Cu with Ag can greatly decrease the ΔG_{RDS} and lower down the kinetic barrier for the vital breakage of N≡N to form *N_2H, which is the rate-determining step (RDS) of the eN_2RR process. As expected, the CuAg-PS alloy exhibits excellent electrocatalytic performance for eN_2RR, giving a high NH_3 yield rate of 38.35 μg h^{-1} cm^{-2} and the FE of 12.72% at − 0.60 V versus RHE in 0.1 M H_2SO_4 solution under ambient condition, which is superior among all reported metal catalysts. Our study provides a feasible strategy for the design of high-performance eN_2RR catalysts and unravels the function and the corresponding mechanism of CuAg-PS alloy interface in CuAg alloy, and finally proves the capability and potential of Cu@CuAg (200)-PS alloy as a highly active electrocatalyst towards electrocatalytic eN_2RR for NH_3 production.

CRediT authorship contribution statement

Zengxi Wei: Conceptualization, Methodology, Writing – original draft, Writing – review & editing, Data curation. **Zhengxiang Gu**: Investigation, Data curation, Writing – original draft. **Yechuan Zhang**: Visualization, Formal analysis. **Kui Luo**: Resources, Supervision, Funding acquisition. **Shuangliang Zhao**: Conceptualization, Writing – review & editing, Supervision, Funding acquisition.

Declaration of Competing Interest

The authors declare that they have no known competing financial interests or personal relationships that could have appeared to influence the work reported in this paper.

Data Availability

No data was used for the research described in the article.

Acknowledgment

Z. Wei and Z. Gu contributed equally to this work. This work is supported by the National Natural Science Foundation of China (91934302, 22178072), the China Postdoctoral Science Foundation (2020M683617XB), the Opening Project of Guangxi Key Laboratory of Petrochemical Resource Processing and Process Intensification Technology (2020K006). Density functional theory calculations are supported by the Guangxi University, Guangxi Postdoctoral Innovative Talents Support Program and Guangxi Science and Technology Base and

Talent Special Project (AD21075015, AD21220017). The authors also would like to thank the Analytical and Testing Center of Sichuan University for morphology characterization work and the authors would be grateful to Dr. Yong Liu for her help of SEM analysis and Dr. Shanling Wang for her assistance on the TEM analysis. This research is also supported by the National Natural Science Foundation of China (51873120, 52073193, 81621003), 1·3·5 project for disciplines of excellence, West China Hospital, Sichuan University (ZYJC21013). The Fundamental Research Funds for the Central Universities (20826041E4067).

Appendix A. Supporting information

Supplementary data associated with this article can be found in the online version at doi:10.1016/j.apcatb.2022.121915.

References

[1] B.H. Suryanto, H.-L. Du, D. Wang, J. Chen, A.N. Simonov, D.R. MacFarlane, Challenges and prospects in the catalysis of electroreduction of nitrogen to ammonia, Nat. Catal. 2 (2019) 290–296.
[2] B.H. Suryanto, K. Matuszek, J. Choi, R.Y. Hodgetts, H.-L. Du, J.M. Bakker, C. S. Kang, P.V. Cherepanov, A.N. Simonov, D.R. MacFarlane, Nitrogen reduction to ammonia at high efficiency and rates based on a phosphonium proton shuttle, Science 372 (2021) 1187–1191.
[3] S. Wu, S.C.E. Tsang, Renewable N-cycle catalysis, Trends Chem. 3 (2021) 660–673.
[4] Y. Zeng, C. Priest, G. Wang, G. Wu, Restoring the nitrogen cycle by electrochemical reduction of nitrate: progress and prospects, Small Methods 4 (2020), 2000672.
[5] R.J. Burford, M.D. Fryzuk, Examining the relationship between coordination mode and reactivity of dinitrogen, Nat. Rev. Chem. 1 (2017).
[6] R. Lan, J.T.S. Irvine, S. Tao, Ammonia and related chemicals as potential indirect hydrogen storage materials, Int. J. Hydrog. Energy 37 (2012) 1482–1494.
[7] X. Cui, C. Tang, Q. Zhang, A review of electrocatalytic reduction of dinitrogen to ammonia under ambient conditions, Adv. Energy Mater. 8 (2018), 1800369.
[8] P. Mehta, P. Barboun, F.A. Herrera, J. Kim, P. Rumbach, D.B. Go, J.C. Hicks, W. F. Schneider, Overcoming ammonia synthesis scaling relations with plasma-enabled catalysis, Nat. Catal. 1 (2018) 269–275.
[9] Z. Wei, Y. Zhang, S. Wang, C. Wang, J. Ma, Fe-doped phosphorene for the nitrogen reduction reaction, J. Mater. Chem. A 6 (2018) 13790–13796.
[10] Z. Wei, Y. Feng, J. Ma, Co-doped graphene edge for enhanced N_2-to-NH_3 conversion, J. Energy Chem. 48 (2020) 322–327.
[11] Z. Wei, J. He, Y. Yang, Z. Xia, Y. Feng, J. Ma, Fe, V-co-doped C_2N for electrocatalytic N_2-to-NH_3 conversion, J. Energy Chem. 53 (2021) 303–308.
[12] X. Yao, Z. Chen, Y. Wang, X. Lang, W. Gao, Y. Zhu, Q. Jiang, Activated basal planes of WS_2 by intrinsic defects as catalysts for the electrocatalytic nitrogen reduction reaction, J. Mater. Chem. A 7 (2019) 25961–25968.
[13] X. Yu, P. Han, Z. Wei, L. Huang, Z. Gu, S. Peng, J. Ma, G. Zheng, Boron-doped graphene for electrocatalytic N_2 reduction, Joule 2 (2018) 1610–1622.
[14] P.-Y. Liu, K. Shi, W.-Z. Chen, R. Gao, Z.-L. Liu, H. Hao, Y.-Q. Wang, Enhanced electrocatalytic nitrogen reduction reaction performance by interfacial engineering of MOF-based sulfides $FeNi_2S_4$/NiS hetero-interface, Appl. Catal. B: Environ. 287 (2021), 119956.
[15] D. Bao, Q. Zhang, F.L. Meng, H.X. Zhong, M.M. Shi, Y. Zhang, J.M. Yan, Q. Jiang, X.B. Zhang, Electrochemical reduction of N_2 under ambient conditions for artificial N_2 fixation and renewable energy storage using N_2/NH_3 cycle, Adv. Mater. 29 (2017), 1604799.
[16] H.-M. Liu, S.-H. Han, Y. Zhao, Y.-Y. Zhu, X.-L. Tian, J.-H. Zeng, J.-X. Jiang, B. Y. Xia, Y. Chen, Surfactant-free atomically ultrathin rhodium nanosheet nanoassemblies for efficient nitrogen electroreduction, J. Mater. Chem. A 6 (2018) 3211–3217.
[17] J. Wang, L. Yu, L. Hu, G. Chen, H. Xin, X. Feng, Ambient ammonia synthesis via palladium-catalyzed electrohydrogenation of dinitrogen at low overpotential, Nat. Commun. 9 (2018) 1–7.
[18] Z. Wang, Y. Li, H. Yu, Y. Xu, H. Xue, X. Li, H. Wang, L. Wang, Ambient electrochemical synthesis of ammonia from nitrogen and water catalyzed by flower-like gold microstructures, ChemSusChem 11 (2018) 3480–3485.
[19] A.R. Singh, B.A. Rohr, J.A. Schwalbe, M. Cargnello, K. Chan, T.F. Jaramillo, I. Chorkendorff, J.K. Norskov, Electrochemical ammonia synthesis-the selectivity challenge, ACS Catal. 7 (2017) 706–709.
[20] J.K. Norskov, T. Bligaard, B. Hvolbaek, F. Abild-Pedersen, I. Chorkendorff, C. H. Christensen, The nature of the active site in heterogeneous metal catalysis, Chem. Soc. Rev. 37 (2008) 2163–2171.
[21] Z.W. Seh, J. Kibsgaard, C.F. Dickens, I.B. Chorkendorff, J.K. Norskov, T. F. Jaramillo, Combining theory and experiment in electrocatalysis: Insights into materials design, Science 355 (2017).
[22] K.D. Gilroy, A. Ruditskiy, H.-C. Peng, D. Qin, Y. Xia, Bimetallic nanocrystals: syntheses, properties, and applications, Chem. Rev. 116 (2016) 10414–10472.
[23] C. Li, H. Tan, J. Lin, X. Luo, S. Wang, J. You, Y.-M. Kang, Y. Bando, Y. Yamauchi, J. Kim, Emerging Pt-based electrocatalysts with highly open nanoarchitectures for boosting oxygen reduction reaction, Nano Today 21 (2018) 91–105.
[24] B.W. Zhang, H.L. Yang, Y.X. Wang, S.X. Dou, H.K. Liu, A comprehensive review on controlling surface composition of Pt-based bimetallic electrocatalysts, Adv. Energy Mater. 8 (2018), 1703597.
[25] M.M. Shi, D. Bao, S.J. Li, B.R. Wulan, J.M. Yan, Q. Jiang, Anchoring PdCu amorphous nanocluster on graphene for electrochemical reduction of N_2 to NH_3 under ambient conditions in aqueous solution, Adv. Energy Mater. 8 (2018), 1800124.
[26] R. Chang, L. Zheng, C. Wang, D. Yang, G. Zhang, S. Sun, Synthesis of hierarchical platinum-palladium-copper nanodendrites for efficient methanol oxidation, Appl. Catal. B: Environ. 211 (2017) 205–211.
[27] C. Li, M. Iqbal, J. Lin, X. Luo, B. Jiang, V. Malgras, K.C.-W. Wu, J. Kim, Y. Yamauchi, Electrochemical deposition: an advanced approach for templated synthesis of nanoporous metal architectures, Acc. Chem. Res. 51 (2018) 1764–1773.
[28] X. Qiu, H. Zhang, P. Wu, F. Zhang, S. Wei, D. Sun, L. Xu, Y. Tang, One-pot synthesis of freestanding porous palladium nanosheets as highly efficient electrocatalysts for formic acid oxidation, Adv. Funct. Mater. 27 (2017), 1603852.
[29] S. Ma, M. Sadakiyo, M. Heima, R. Luo, R.T. Haasch, J.I. Gold, M. Yamauchi, P. J. Kenis, Electroreduction of carbon dioxide to hydrocarbons using bimetallic Cu-Pd catalysts with different mixing patterns, J. Am. Chem. Soc. 139 (2017) 47–50.
[30] B. Jiang, C. Li, V. Malgras, M. Imura, S. Tominaka, Y. Yamauchi, Mesoporous Pt nanospheres with designed pore surface as highly active electrocatalyst, Chem. Sci. 7 (2016) 1575–1581.
[31] Y.-M. Lin, C.-Y. Lee, Y.-L. Chen, C.-P. Pan, C.-E. Ho, Significantly improving the mechanical/electrical characteristics of blind-hole Cu filling through crystal coherent modification, Surf. Coat. Technol. (2022), 128111.
[32] C. Zhu, Q. Shi, S. Fu, J. Song, H. Xia, D. Du, Y. Lin, Efficient synthesis of MCu (M= Pd, Pt, and Au) aerogels with accelerated gelation kinetics and their high electrocatalytic activity, Adv. Mater. 28 (2016) 8779–8783.
[33] P. Wang, W. Nong, Y. Li, H. Cui, C. Wang, Strengthening nitrogen affinity on CuAu@Cu core–shell nanoparticles with ultrathin Cu skin via strain engineering and ligand effect for boosting nitrogen reduction reaction, Appl. Catal. B: Environ. 288 (2021), 119999.
[34] R. Shi, N. Ma, Y. Wang, Predicting equilibrium shape of precipitates as function of coherency state, Acta Mater. 60 (2012) 4172–4184.
[35] M. Chandross, Energetics of the formation of Cu–Ag core–shell nanoparticles, Model. Simul. Mater. Sci. 22 (2014), 075012.
[36] W.T. Osowiecki, X. Ye, P. Satish, K.C. Bustillo, E.L. Clark, A.P. Alivisatos, Tailoring morphology of Cu–Ag nanocrescents and core–shell nanocrystals guided by a thermodynamic model, J. Am. Chem. Soc. 140 (2018) 8569–8577.
[37] X. Kong, I.J. Beyerlein, Z. Liu, B. Yao, D. Legut, T.C. Germann, R. Zhang, Stronger and more failure-resistant with three-dimensional serrated bimetal interfaces, Acta Mater. 166 (2019) 231–245.
[38] N. Mara, I. Beyerlein, J. Carpenter, J. Wang, Interfacially driven deformation twinning in bulk Ag-Cu composites, JOM 64 (2012) 1218–1226.
[39] I.J. Beyerlein, M.J. Demkowicz, A. Misra, B. Uberuaga, Defect-interface interactions, Prog. Mater. Sci. 74 (2015) 125–210.
[40] G. Kresse, J. Hafner, Ab initio molecular dynamics for liquid metals, Phys. Rev. B 47 (1993) 558.
[41] P.E. Blöchl, Projector augmented-wave method, Phys. Rev. B 50 (1994) 17953.
[42] G. Kresse, J. Furthmüller, Efficiency of ab-initio total energy calculations for metals and semiconductors using a plane-wave basis set, Comp. Mater. Sci. 6 (1996) 15–50.
[43] S. Grimme, J. Antony, S. Ehrlich, H. Krieg, A consistent and accurate ab initio parametrization of density functional dispersion correction (DFT-D) for the 94 elements H-Pu, J. Chem. Phys. 132 (2010), 154104.
[44] M. Hÿtch, E. Snoeck, R. Kilaas, Quantitative measurement of displacement and strain fields from HREM micrographs, Ultramicroscopy 74 (1998) 131–146.
[45] A. Dutta, I.Z. Montiel, R. Erni, K. Kiran, M. Rahaman, J. Drnec, P. Broekmann, Activation of bimetallic AgCu foam electrocatalysts for ethanol formation from CO_2 by selective Cu oxidation/reduction, Nano Energy 68 (2020), 104331.
[46] J. Terblans, Calculating the bulk vacancy formation energy (Ev) for a Schottky defect in a perfect Cu (111), Cu (100) and a Cu (110) single crystal, surface and interface analysis: an international journal devoted to the development and application of techniques for the analysis of surfaces, Interfaces Thin films 33 (2002) 767–770.
[47] L. Zhang, L.X. Ding, G.F. Chen, X. Yang, H. Wang, Ammonia synthesis under ambient conditions: selective electroreduction of dinitrogen to ammonia on black phosphorus nanosheets, Angew. Chem. 131 (2019) 2638–2642.
[48] Z.-Y. Zhou, N. Tian, Z.-Z. Huang, D.-J. Chen, S.-G. Sun, Nanoparticle catalysts with high energy surfaces and enhanced activity synthesized by electrochemical method, Faraday Discuss. 140 (2008) 81–92.